PHYSICAL REVIEW MATERIALS **6**, 124409 (2022)

Editors' Suggestion

Spin-wave study of magnetic perpendicular surface anisotropy in single crystalline MgO/Fe/MgO films

J. Solano,[1] O. Gladii,[2] P. Kuntz,[3] Y. Henry,[1] D. Halley,[1] and M. Bailleul[1,*]

[1]*Institut de Physique et Chimie des Matériaux de Strasbourg, UMR 7504 CNRS, Université de Strasbourg, 23 rue du Loess, BP 43, 67034 Strasbourg Cedex 2, France*

[2]*Helmholtz-Zentrum Dresden - Rossendorf, Institute of Ion Beam Physics and Materials Research, 01328 Dresden, Germany*

[3]*Entroview, 11 rue des mathématiques, 38402 Saint Martin d'Hères, France*

(Received 2 September 2022; accepted 2 December 2022; published 20 December 2022)

Broadband ferromagnetic resonance is measured in single crystalline Fe films of varying thickness sandwiched between MgO layers. An exhaustive magnetic characterization of the films (exchange constant, cubic, uniaxial and surface anisotropies) is enabled by the study of the uniform and the first perpendicular standing spin wave modes as a function of applied magnetic field and film thickness. Additional measurements of nonreciprocal spin-wave propagation allow us to separate each of the two interface contributions to the total surface anisotropy. The results are consistent with the model of a quasi-bulk film interior and two magnetically different top and bottom interfaces, a difference ascribed to different oxidation states.

DOI: 10.1103/PhysRevMaterials.6.124409

I. INTRODUCTION

In recent years, there has been an increased interest in magnetic films with large perpendicular magnetic anisotropy due to their potential to improve the efficiency and nonvolatility of spin transfer torque magnetoresistive random access memories [1–5]. In this search for new materials, Fe films interfaced with MgO are of particular interest due to their favorable properties: a small magnetic damping, a high tunneling magnetoresistance and a large perpendicular surface anisotropy (PSA) [2,3,6–8].

There is a good general agreement between experimental and theoretical investigations on the nature and order of magnitude of this PSA, with values ranging between 0.86 and 3.15 $\mathrm{mJ/m^2}$ [3,8–17]. These are up to two times larger than usual PSA found at the interfaces between transition metals and heavy metals [6,7,18] despite weak spin-orbit coupling [15]. Theoretical papers have attributed this large PSA to the hybridization between interfacial oxygen and iron atoms [13,14].

Experimentally, it is very challenging to access the internal magnetic environment of ultrathin films and separate the contributions of the top and bottom interfaces to the total PSA of a film. So far, experimental characterizations [3,8–12,19–21] have relied on magnetometry measurements to estimate the surface magnetic anisotropy. This means that additional hypothesis were needed to extract the individual surface anisotropies, including comparison with a reference interface or assumptions regarding possible bulk magnetoelastic contributions.

In this paper, we separate the top and bottom perpendicular surface anisotropies of single crystalline MgO/Fe/MgO films resorting exclusively to spectroscopic measurements of inhomogeneous magnetization dynamics. To achieve this, we perform a broadband ferromagnetic resonance characterization of a thickness series of films MgO/Fe(t)/MgO ($t=$ 10–30 nm) and combine it with a careful study of nonreciprocal spin wave propagation. Our results show that the films of the entire series behave as a quasi-bulk film interior with two Fe/MgO interfaces that are not magnetically equivalent. We deduce then different top and bottom surfaces anisotropies that are in good agreement with theoretical calculations for ultrathin films [13–17]. This paper not only presents a new characterization methodology, but also provides evidence that the large PSA of the technologically relevant ultrathin films also exists in the thicker films traditionally used in material science.

II. BROADBAND FERROMAGNETIC RESONANCE

A. Film growth

The studied films were grown by molecular beam epitaxy on commercial MgO(001) substrates and consist of the following stacks: substrate/MgO(20)/Fe(t)/MgO(8)/Ti(4.5) (thicknesses in nm). The MgO buffer film was deposited on top of a polished MgO surface at 550 °C. The Fe film, with thickness t = 10, 15, 20, 25, 30 nm, was subsequently grown at 100 °C (stair-step structure obtained with a movable shutter). Finally, the sample was annealed at 480 °C and capped with the MgO and Ti layers, both grown at room temperature. The epitaxial relationship between Fe and MgO is such that the [010] and [100] in-plane directions (magnetic easy axes of the Fe film) are rotated by 45° with respect to those of the MgO films (aligned with the edges of the substrate).

The crystalline quality of the samples was confirmed in-situ by RHEED. After growth, an x-ray diffraction study

---

[*] matthieu.bailleul@ipcms.unistra.fr

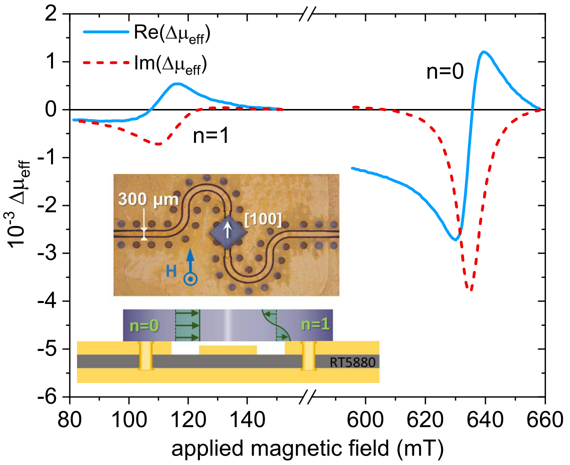

FIG. 1. Ferromagnetic resonance spectrum measured at 40 GHz for the t = 20 nm film. The main panel shows the real and imaginary components of the change of effective permeability as function of the in-plane applied magnetic field (along an the [100] direction of Fe). One distinguishes both a main peak (uniform resonance, $n = 0$) and a satellite one (perpendicular standing spin wave, $n = 1$). The inset contains a photograph of the CPW loaded with a sample at its center (top) and a cross-section sketch showing the tapered CPW, the magnetic film, and the thickness profiles of the dynamic magnetization for the two resonance modes (bottom, not to scale).

revealed a slight tetragonal distortion of the Fe lattice with respect to the bulk, more precisely a 0.5% out-plane compression accompanied by a 0.7% in-plane expansion [22].

B. Vector network analyzer—Ferromagnetic resonance

The dynamic magnetic properties of the films are characterized by Vector Network Analyzer - Ferromagnetic Resonance. The sample (1.8×1.8 mm^2 piece cut from a film) lies on a 50 Ω channelized coplanar waveguide (CPW) [23] with a 300-μm center line separated from the lateral ground planes by 100 μm gaps (see inset in Fig. 1). The 50-μm thick copper/gold top metallization rests on a 127-μm thick PTFE/glass Rogers RT5880 substrate backed with a very thick copper layer. The CPW's top and bottom grounds are connected through rows of vias parallel to the center line in order to ensure a single-mode propagation in the entire 0–50 GHz frequency range. The part of the waveguide on which the sample is placed has a tapered center line (width 200 μm, thickness 30 μm) that compensates for the impedance change caused by the presence of the conductive film on top of the CPW [24].

To perform the magnetic measurements, the CPW and sample are inserted in the gap of an electromagnet and connected to a 2-port vector network analyzer via 2.4 mm connectors and coaxial microwave cables. The analyzer can excite and measure the microwave response of the CPW: microwave reflection on each port and transmission between the two ports. The excitation of the ferromagnetic sample results in a modification of the waveguide's impedance. After a suitable calibration and deembedding procedure [25], we extract the magnetic field-induced change of the effective permeability $\Delta\mu_{\text{eff}}$ of the waveguide loaded with the ferromagnetic sample. This magnetic response exhibits clear resonances when the microwave frequency matches the field-dependent magnetization precession frequency.

Figure 1 shows the ferromagnetic resonance spectrum measured on a 20-nm-thick Fe film at a microwave frequency of 40 GHz with an external field **H** applied in-plane, along the [100] magnetic easy axis (see Fig. 1 inset). One recognizes an intense peak centered at 634 mT, which we attribute to the uniform resonance mode ($n = 0$ in the inset of Fig. 1). A satellite peak centered at 112 mT is also observed: We attribute this to the first perpendicular standing spin wave mode, corresponding to an inhomogeneous precession across the film thickness, with opposite phases at the two surfaces and zero amplitude at the center ($n = 1$ in the inset of Fig. 1). The observation of this satellite peak might be surprising at first glance since the microwave magnetic field produced by the coplanar waveguide is expected to be homogeneous over the thickness of the magnetic film, thus preventing the excitation of inhomogeneous modes. However, the fact that the ferromagnetic film is conductive leads to the occurrence of electromagnetic shielding. This effect is characterized by the creation of electrical currents in the metallic film, which tend to confine the electromagnetic field within the space between the waveguide and the sample [24]. This results in a very inhomogeneous microwave magnetic field distribution across the ferromagnetic film thickness leading to the excitation of nonuniform magnetization precession modes [26].

Similarly, ferromagnetic resonance spectra are recorded for the various thicknesses of Fe with frequency in the range 1.4–50 GHz and external field (up to 2.7 T) applied either in-plane, along the [100] direction of Fe, or out-of-plane (along [001]). Each resonance spectrum is fitted with a complex Lorentzian function. From these fits we extract the resonance fields of the two modes, in the two field configurations (Fig. 2). From the fit of the resonance peak of mode $n = 0$ in the out-of-plane configuration, we also extract the linewidth and from its frequency dependence we finally estimate the damping factor $\alpha = 2.6 \times 10^{-3}$. It must be noted that mode $n = 1$ could not be observed for $t = 10$ nm and 15 nm with in-plane applied field and for $t = 10$ nm with out-of-plane field because the corresponding resonance frequencies lie beyond the 50 GHz experimental limit.

C. Theoretical model

To interpret the resonance data of Fig. 2, we use the so-called Kittel formulas [27]. These simple expressions are known to be exact in the case of a uniform resonance mode in a high-symmetry configuration (equilibrium magnetization parallel or perpendicular to the anisotropy axes). This section shows how they can be extended also to the case of inhomogeneous dynamics ($n = 1$) in films with moderate thickness and sizable surface anisotropies. Our starting point is the linearized Landau-Lifshitz equation for plane spin waves,

$$i\omega\mathbf{m} = \gamma\mu_o(\mathbf{H}_{\text{eq}} \times \mathbf{m} - \mathbf{M}_{\text{eq}} \times \mathbf{h}). \tag{1}$$

Here, ω is the angular frequency, γ is the gyromagnetic ratio and μ_0 is the permeability of vacuum. $\mathbf{M}_{\text{eq}}$ and $\mathbf{m}$ are the static and dynamic components of the magnetization,

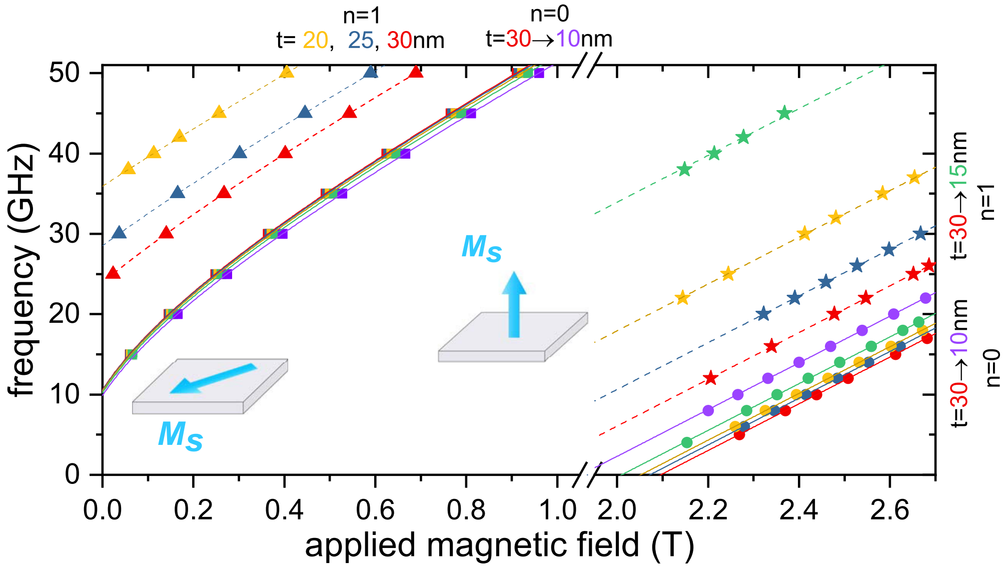

FIG. 2. Measured frequency vs resonance magnetic field of both the uniform mode ($n = 0$) and first perpendicular standing spin wave mode ($n = 1$) for the entire thickness series. In the case of in-plane applied field, squares (triangles) correspond to mode $n = 0$ ($n = 1$). For the case of out-of-plane applied field, circles (stars) correspond to mode $n = 0$ ($n = 1$). The lines are the corresponding Kittel fits [see Eqs. (5)].

respectively. Similarly, $\mathbf{H}_{\mathrm{eq}}$ and $\mathbf{h}$ are the static and dynamic parts of the effective magnetic field, respectively. The effective field derives from the total magnetic energy [28], which in the present case contains five contributions: (i) the exchange and (ii) demagnetizing contributions present in any ferromagnet, (iii) the cubic volume anisotropy known to exist in iron, (iv) surface perpendicular anisotropies at the two Fe/MgO interfaces, and (v) an additional volume anisotropy with uniaxial symmetry and perpendicular-to-plane axis, which, we argue, is created by strain through a magnetoelastic coupling (see Sec. IV).

When the external magnetic field $\mathbf{H}$ is applied along the easy axes of the Fe films, the static effective field writes

$$H_{\mathrm{eq}}(\xi) = \begin{cases} H & \text{if } \mathbf{H} \parallel [100]_{\mathrm{Fe}} \\ H + H_{\mathrm{U}} + h_{\mathrm{S}}(\xi) - M_{\mathrm{s}} & \text{if } \mathbf{H} \parallel [001]_{\mathrm{Fe}}, \end{cases} \tag{2}$$

while the dynamic effective field writes

$$\mathbf{h} = \frac{1}{M_{\mathrm{s}}}\left\{\left[\frac{2A}{\mu_0 M_{\mathrm{s}}}\nabla^2 + H_{\mathrm{K}}\right]\mathbf{m} + [H_{\mathrm{U}} + h_{\mathrm{S}}(\xi) - M_{\mathrm{s}}]m_\xi \hat{\boldsymbol{\xi}}\right\}. \tag{3}$$

Here, M_{s} is the saturation magnetization, A is the exchange stiffness constant, $\hat{\boldsymbol{\xi}}$ is a unit vector along the direction perpendicular to the film and m_ξ is the dynamic magnetization component along this direction. Additionally, $H_{\mathrm{K}} = \frac{2K_1}{\mu_0 M_{\mathrm{s}}}$, where K_1 is the volume cubic anisotropy constant, and $H_{\mathrm{U}} = \frac{2K_{\mathrm{U}}}{\mu_0 M_{\mathrm{s}}}$, where K_{U} is the volume uniaxial magnetoelastic anisotropy constant. Finally, the field $h_{\mathrm{s}}(\xi) = \frac{2}{\mu_0 M_{\mathrm{s}}}[K_{\mathrm{S}}^{\mathrm{bot}}\delta(\xi) + K_{\mathrm{S}}^{\mathrm{top}}\delta(\xi - t)]$ models the perpendicular surface anisotropies with constants $K_{\mathrm{S}}^{\mathrm{top}}$ and $K_{\mathrm{S}}^{\mathrm{bot}}$ at the top and bottom interfaces, respectively [29]. Note that $m_\xi = 0$ when a saturating magnetic field is applied perpendicular to the plane of the film ($\mathbf{M}_{\mathrm{eq}} \parallel \hat{\boldsymbol{\xi}}$), making Eq. (3) valid for the two experimental configurations considered in Eq. (2).

The system of equations (1)–(3) is effectively a fourth-order differential equation for the dynamic magnetization with mixed-type boundary conditions (so-called surface pinning), which does not have an exact analytical solution [30]. However, it is possible to obtain approximate solutions in some limiting cases. In particular, if the exchange energy A/t is much larger than the surface anisotropy K_{S}, we can expand the dynamic magnetization in a Fourier series of cosine thickness modes (unpinned standing spin wave modes) and, in the spirit of the Kalinikos-Slavin theory of dipole-exchange spin waves [31,32], limit ourselves to the first two terms of the series. Then we may write the complex amplitude of the dynamic magnetization $\mathbf{m}^*(\xi)$ as

$$\mathbf{m}^*(\xi) = \left[m_x^0\Phi_0 + m_x^1\Phi_1(\xi)\right]\hat{\boldsymbol{x}} + \left[m_y^0\Phi_0 + m_y^1\Phi_1(\xi)\right]\hat{\boldsymbol{y}}, \tag{4}$$

with x and y denoting two directions orthogonal to the static magnetization $\mathbf{M}_{\mathrm{eq}}$. $\Phi_0 = 1/\sqrt{t}$ is the lowest order term in the Fourier series corresponding to a normalized uniform distribution, and $\Phi_1(\xi) = \sqrt{2}\cos(\frac{\pi}{t}\xi)/\sqrt{t}$ is the second term corresponding to a normalized nonuniform distribution with a thickness-profile, which is antisymmetric with respect to the center of the film (see their sketch in the inset of Fig. 1). In the basis of the four orthogonal vector modes $[\Phi_0\hat{\mathbf{x}},\ \Phi_1(\xi)\hat{\mathbf{x}},\ \Phi_0\hat{\mathbf{y}},\ \Phi_1(\xi)\hat{\mathbf{y}}]$, the complex amplitude of the dynamic magnetization can be conveniently expressed as $\mathbf{m}^* = (m_x^0, m_x^1, m_y^0, m_y^1)$.

After substituting Eqs. (3) and (4) in Eq. (1), one can project the system of equations (1)–(3) on this new four-mode basis (see Ref. [33] for a detailed treatment of the projection) and obtain a simplified eigenvalue equation of the form $i\omega\mathbf{m}^* = C\mathbf{m}^*$, where C is the 4×4 dynamic matrix [29]. The eigenvalues of this matrix are the resonance frequencies. By replacing the eigenvectors of matrix C back in Eq. (4) one may recover the actual oscillation modes of the magnetization.

The dynamic matrix in the presence of surface anisotropies is given in Appendix A for the case of a spin wave with wave vector $\mathbf{k}$ parallel to the $[010]_{\mathrm{Fe}}$ axis. It is important to note that this matrix depends explicitly not only

TABLE I. Explicit expressions of stiffness fields in the resonance frequencies of Eqs. (5).

Field	$n = 0$	$n = 1$
H_{Xn}	H_K	$H_K + H_E$
H_{Yn}	$M_s + H_K - H_U - H_S$	$M_s + H_K - H_U - 2H_S + H_E$
H_{Zn}	$M_s - H_K - H_U - H_S$	$M_s - H_K - H_U - 2H_S - H_E$

on the total surface anisotropy $K_S = K_S^{\text{bot}} + K_S^{\text{top}}$ but also on the difference of surface anisotropies at the two interfaces $\Delta K_S = K_S^{\text{bot}} - K_S^{\text{top}}$ [29].

Let us now concentrate on the case of ferromagnetic resonance ($k = 0$). Up to first order in ΔK_S, our approach produces Kittel-like [27] expressions for the resonance frequencies of the first two standing spin wave modes,

$$f_{\parallel n} = \frac{\gamma\mu_0}{2\pi}[(H + H_{Xn})(H + H_{Yn})]^{1/2}, \tag{5a}$$

$$f_{\perp n} = \frac{\gamma\mu_0}{2\pi}(H - H_{Zn}). \tag{5b}$$

Here $n = 0, 1$ is the mode index, and $\parallel$ and $\perp$ refer to the configurations with $\mathbf{H} \parallel [100]_{\text{Fe}}$ and $\mathbf{H} \parallel [001]_{\text{Fe}}$, respectively. $H_{\alpha n}$ are orientation and mode-dependent stiffness fields whose expressions are given in Table I, where the following thickness-dependent exchange and surface anisotropy fields have been used,

$$H_E = \frac{2\pi^2 A}{\mu_0 M_s t^2}, \tag{6a}$$

$$H_S = \frac{2K_S}{\mu_0 M_s t}. \tag{6b}$$

At the chosen level of approximation, which is valid only for small differences in surface anisotropies ($\Delta K_S\, t/A \ll 1$), the resonance frequencies [Eqs. (5)] depend on K_S but not on ΔK_S, although the C matrix depends explicitly on it. This may be explained as follows. With $k = 0$, the mutual demagnetization factor Q vanishes (see Appendix A) and so does the largest source of hybridization between the uniform and antisymmetric basis modes. Only terms in ΔK_S remain nonzero in the off diagonal blocks of the C matrix [Eq. (A1)], meaning that the difference in surface anisotropies becomes the sole source of hybridization. It happens that the corresponding coupling is proportional to ΔK_S^2 and is thus neglected in the above approximation. We note also that the contribution of surface anisotropies to the stiffness fields is doubled in the case of mode $n = 1$ as compared to mode $n = 0$. This is a direct consequence of mode $n = 0$ being uniform at this level of approximation while mode $n = 1$ is fully asymmetric with large amplitude at the surfaces, which makes it more sensitive to PSA.

D. Results

Fitting the experimental data in Fig. 2 to the corresponding Eqs. (5) yields the values of the stiffness fields H_{Xn}, H_{Yn}, and H_{Zn} ($n = 0, 1$) presented in Fig. 3 as open circles. For this extraction, we assume a unique value for γ (see Table II), which is the average over all film thicknesses of the individual γ values obtained by fitting $f_{\perp 0}(H)$ experimental data to Eq. (5b).

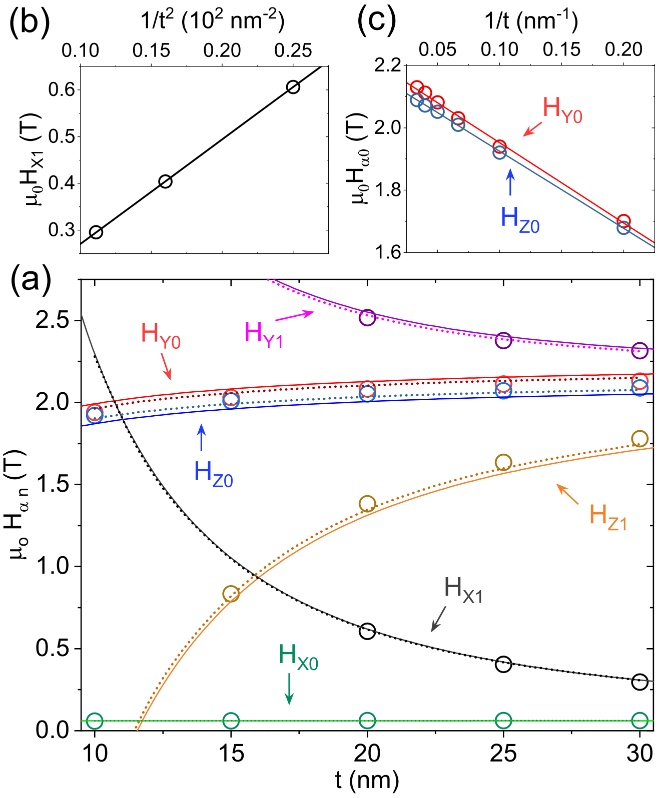

FIG. 3. (a) Stiffness fields as a function of Fe thickness obtained from Kittel-like fits of the experimental resonance frequencies (open circles) compared with the analytical model of Table I (solid lines) and the values obtained from Kittel-like fits of SWIIM simulations (dotted lines). (b) Stiffness field H_{X1} as a function of $1/t^2$. (c) Stiffness fields H_{Y0} and H_{Z0} as a function of $1/t$.

Values of the stiffness fields associated with the two oscillation modes ($n = 0, 1$) can be readily treated and combined sequentially so as to extract most of the magnetic parameters of the iron films. As a starting point and in agreement with SQUID characterization, the saturation magnetization value is set to that of bulk iron $\mu_0 M_s = 2.15$ T. Next, we observe that H_{X0} is thickness independent and we extract the cubic anisotropy constant K_1 from $H_{X0} = H_K$. Then, since $H_{X1} - H_{X0} = H_E$ varies as t^{-2} [Fig. 3(b)], we confidently extract a thickness independent exchange constant A [Eq. (6a)]. We subsequently notice that the thickness

TABLE II. Magnetic parameters obtained for MgO/Fe(t)/MgO films ($t = 10-30$ nm).

$\mu_0 M_s$ [T]	$\gamma/2\pi$ [GHz/T]	A [pJ/m]	K_1 [kJ/m^3]
2.15[a]	29.1 ± 0.6	19.4 ± 0.1	52 ± 1
K_U [kJ/m^3]	K_S [mJ/m^2]	ΔK_S [mJ/m^2]	
-45 ± 28	2.3 ± 0.3	0.8[b]± 0.1	

[a] Tabulated value for bulk iron at room temperature.

[b] Value obtained from nonreciprocal spin wave measurements (See Section III).

dependent parts of H_{Y0} and H_{Z0} both vary as t^{-1}, with similar slopes [Fig. 3(c)], from which we determine the average total surface anisotropy constant K_S [Eq. (6b)]. Finally, we determine the uniaxial anisotropy constant K_U using $H_{Y0}+H_{Z0}-2(M_s-H_S)=2H_U$.

The obtained magnetic parameters are summarized in Table II. In the chosen parametrization, the negative sign of K_U indicates an easy-plane parallel to the film's plane and the positive sign of K_S an easy axis along the film normal.

The lines in Fig. 3 are the theoretical stiffness fields calculated by injecting the parameters just determined (Table II) back into our analytical model. The good agreement obtained illustrates that a single set of thickness independent magnetic parameters is indeed enough to capture most features of the magnetization dynamics in the studied MgO/Fe/MgO films. Furthermore, the fact that the agreement also applies to those stiffness fields which have not been considered in the above analysis (H_{Y1} and H_{Z1}) can be considered as a validation of the model. There are however points of slight disagreement between the experimentally determined values and the corresponding analytical predictions. In particular, predicted values of the difference $H_{Y0}-H_{Z0}$ are significantly larger than the ones determined experimentally. As may be inferred from Appendix B, modifying the analytical model [Eqs. (5)] to include terms up to second order in ΔK_S allows one partially reducing the disagreement. This second-order approximation however produces cumbersome expressions which are unpractical and, even more importantly, unable to provide information regarding the sign of ΔK_S. This points at the need for an accurate determination of this additional parameter through an experimental technique, which is sensitive to it at first order, namely spin wave frequency nonreciprocity.

III. NONRECIPROCAL SPIN WAVE PROPAGATION

Propagating spin wave spectroscopy has been shown to be very sensitive to magnetic asymmetries across the thickness of thin films [29], including differences in surface anistropies at the two interfaces ($\Delta K_S \neq 0$). The principle of such measurement is sketched in the inset of Fig. 4. A spin wave propagating in the so-called Damon-Eshbach geometry (i.e., with its wave vector **k** oriented perpendicular to the in-plane applied magnetic field **H**) is known to exhibit a mode profile nonreciprocity. This means that the wave has an asymmetric distribution across the film thickness, with more amplitude on one side of the film than on the other. This asymmetric profile is reversed when changing the sign of **k**, i.e., for spin waves propagating in the opposite direction [34] (see inset of Fig. 4). Consequently, an inhomogeneous magnetic environment across the thickness will have different effects on the dynamics of counterpropagating spin waves. This can be measured experimentally as a difference between their resonance frequencies, which becomes a spectroscopic signature of the film's asymmetric magnetic environment [29].

To measure this frequency nonreciprocity, suitable devices are fabricated from the Fe samples. This is achieved by patterning the film into a strip geometry and fabricating a pair of conductors on top. These conductors with a meander geometry serve as antennas for exciting and detecting spin waves of controlled wavelength. With the design chosen in the present paper (see inset in Fig. 4) the most important excitation occurs around two particular wave vectors $k_1 = 3.9\,\mathrm{rad}/\mu\mathrm{m}$ and $k_2 = 1.57\,\mathrm{rad}/\mu\mathrm{m}$. By using two separate antennas, and interchanging their role, it is possible to measure the changes in mutual inductance corresponding to spin waves propagating with positive and negative wave vectors $\Delta L_{k>0}$, $\Delta L_{k<0}$ [35]. More details on the fabrication process of the devices and experimental procedure can be found elsewhere [36].

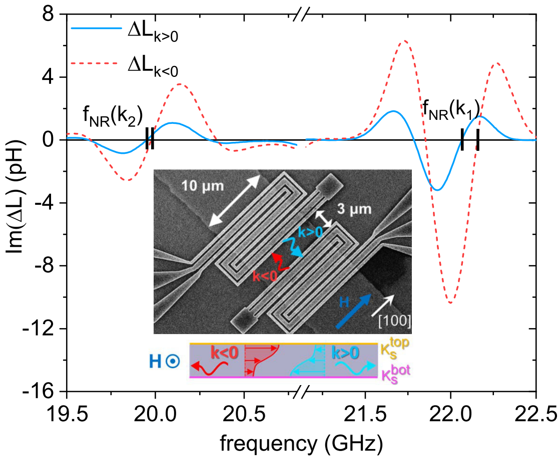

FIG. 4. Measured imaginary component of the mutual inductance between antennas due to counterpropagating spin waves (with wave numbers: $k_1 = 3.9\,\mathrm{rad}/\mu\mathrm{m}$ and $k_2 = 1.57\,\mathrm{rad}/\mu\mathrm{m}$) in a strip of $t = 20$ nm Fe film under a 120-mT magnetic field (Damon-Eshbach geometry). The inset shows an electronic microscope image of the experimental device (top) and a sketch of the asymmetric modal profiles of counterpropagating waves across the thickness of the film and its interplay with asymmetric magnetic surface anisotropies (bottom).

Figure 4 shows the measured change in mutual inductance corresponding to spin wave propagation in a $t = 20$-nm device under a 120-mT field applied along [100]. One can observe directly a frequency difference between counterpropagating waves, both for the main spin wave excitation [$f_{\mathrm{NR}}(k_1)$] and for the secondary one [$f_{\mathrm{NR}}(k_2)$]. The value of this frequency nonreciprocity is followed as a function of the applied magnetic field in the range 30–200 mT. The different symbols in Fig. 5 show the frequency nonreciprocity measured for three different samples: namely devices from the FMR series with $t = 10$ nm and 20 nm, and a third device with $t = 20$ nm but without Ti capping, labeled thereafter 20 nm*. We observe that f_{NR} is roughly field independent.

To analyze quantitatively the data in Fig. 5 and estimate the difference in magnetic surface anisotropy ΔK_S, we use the theory developed in the previous section with some modifications. To account for the propagating character of the spin waves, the space-dependent part of the dynamic component of the magnetization [Eq. (4)] becomes $\mathbf{m}^*(\xi)e^{-ik\eta}$ where $\hat{\eta}$ is a direction vector along the ferromagnetic strip. Now, the

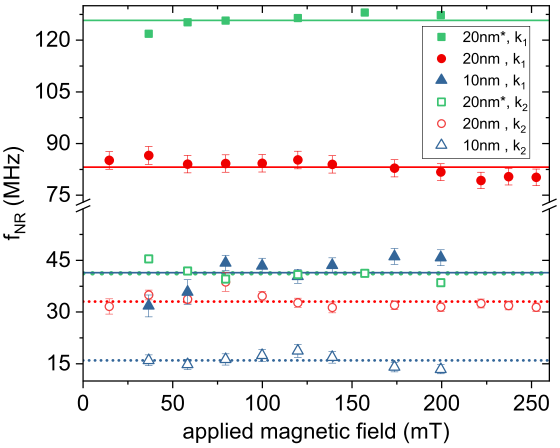

FIG. 5. Frequency nonreciprocity measurements as a function of applied magnetic field for devices $t = 10$ nm, 20 nm, and 20 nm* and each wave numbers $k_1 = 3.9$ rad/μm, $k_2 = 1.57$ rad/μm. The lines correspond to the average value of f_{NR} over the experimental field range.

dynamic magnetic field writes

$$\mathbf{h} = \frac{1}{M_s}\left\{\left[\frac{2A}{\mu_0 M_s}\nabla^2 + H_K\right]\mathbf{m} + [H_U + h_s(\xi)]m_\xi\hat{\boldsymbol{\xi}}\right\} + \int_0^t G_k(\xi - \xi')\mathbf{m}\, d\xi', \tag{7}$$

where the last term is the dipolar contribution and G_k the magnetostatic Green's tensor [37]. As in the previous section, the system of Eqs. (1) and (7) can be projected onto the spin wave modes basis, which allows one to obtain an eigenvalue equation with a dynamical matrix C given explicitly in Appendix A (note that in this case $k \neq 0$). In the Damon-Eshbach configuration, the nonuniform character of magnetization along $\hat{\eta}$ gives rise to dipolar coupling between Fourier components $n = 0$ and $n = 1$ [through the factor $Q \neq 0$ in the nondiagonal blocks of the dynamic matrix C, see Eq. (A1a)], which is nonreciprocal with respect to the wave number. This, combined with the asymmetry produced by ΔK_S, is at the very origin of the frequency nonreciprocity.

Once again we can calculate the resonance frequencies from the dynamic matrix C, and in this case, obtain the frequency difference between counterpropagating waves. Assuming $\Delta K_S t/A \ll 1$, an approximate expression can be derived in which the frequency nonreciprocity of mode $n = 0$ is a linear function of both the wave number k and the difference in surface anisotropy ΔK_S [29],

$$f_{NR} = f_{\parallel 0}(k < 0) - f_{\parallel 0}(k > 0) \approx \frac{8\gamma\, \Delta K_S}{\pi^3 M_s\left(1 + \frac{\Lambda^2\pi^2}{t^2}\right)}k. \tag{8}$$

Since f_{NR} shows no systematic variation with the external magnetic field (Fig. 5), we consider below its average value over the 30–200 mT range and plot it in Fig. 6 as a function of k for each of the studied films. Applying Eq. (8) and using values of γ, M_s, and A found in Table II, we finally extract estimates for ΔK_S from the slopes of linear fits: 0.8, 1.1, 1.6 mJ/m^2 for the 10 nm, 20 nm, and 20 nm* films, respectively.

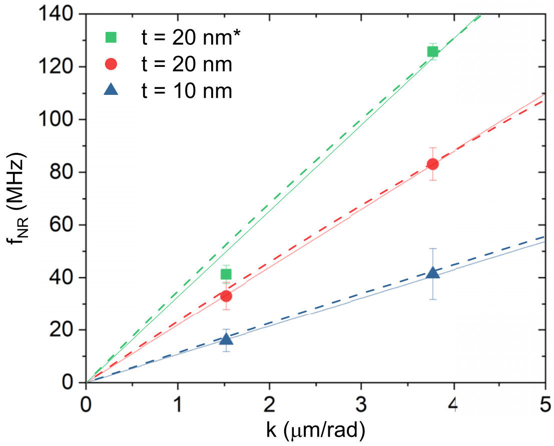

FIG. 6. Frequency nonreciprocity as a function of wave number for the three films under study. The points represent the average experimental values in the applied field range 30–200 mT (see Fig. 5). The solid lines are the corresponding linear fits to Eq. (8). The dashed lines show the mean value as calculated with SWIIM while using values for ΔK_S that best adjust the experimental points (see text for details).

These results confirm the asymmetry of the two film interfaces suggested by FMR measurements. They show that ΔK_S is undoubtedly positive, which means that, in all films, the bottom interface has a stronger PSA than the top one. Since the above characterization is based on several approximations [Eqs. (4) and (8)], the magnitude of ΔK_S should however be refined before comparing and contrasting the films and their respective interfaces. To this aim, we finally turn to numerical simulations.

We resort to the code SWIIM [38], which provides a finite-difference numerical solution of Eqs. (1) and (7) to calculate the difference between the frequencies of counterpropagating waves as a function of wave number k in the Damon-Eshbach configuration. For each sample, we adjust ΔK_S (the remaining magnetic parameters are taken from Table II), so as to best reproduce the experimental $k_{NR}(k)$ data in Fig. 6 (dashed lines). The values of ΔK_S obtained in this way are 0.7, 0.8, and 1.2 mJ/m^2 for the 10 nm, 20 nm, and 20 nm* films, respectively. Comparing them with values obtained from Eq. (8), we observe that the analytical approach systematically underestimates the effect of $\Delta K_S \neq 0$. Noticeably, using numerical simulations allows us reducing the difference between the values of ΔK_S for the 10 nm and 20 nm samples to almost nothing, which is of course expected for films of similar composition. We then choose the value $\Delta K_S = 0.8$ mJ/m^2 as a reference for our MgO/Fe/MgO system.

Having refined the magnitude of ΔK_S, we finally go back to the ferromagnetic resonance case and we use SWIIM to calculate the resonance frequencies of the two lowest FMR modes as a function of magnetic field using the now completed set of magnetic parameters (Table II). Then we fit the frequencies determined numerically to Eqs. (5) and extract the corresponding stiffness fields. As expected, accounting for the difference in surface anisotropy evidenced through propagating spin wave spectroscopy allows one improving slightly the agreement between experimentally and numerically determined H_{Y0}, H_{Z0}, H_{Y1}, and H_{Z1} stiffness fields (Fig. 3). Note that despite the introduction of ΔK_S and the exact treatment of hybridization effects by SWIIM, numerical data remain however rather close to predictions of our analytical model. This proves the suitability of our choice of a limited four-vector mode basis (Sec. II C).

IV. DISCUSSION

Starting from a simplified analytical model, we have described above a method for extracting the magnetic parameters of ferromagnetic films with moderate thickness from broadband ferromagnetic resonance and propagating spin wave spectroscopy measurements. The positions of the ferromagnetic resonance peaks measured over large field and frequency ranges are first fitted to Kittel formulas (Fig. 2). Then, the extracted stiffness fields are confronted to explicit expressions (Table I) allowing one to extract successively five magnetic parameters. The deviations between the model and the experiments do not exceed 3% (Fig. 3), which we find very satisfactory given the wide range of field, frequency and film thickness investigated, and the limited number of parameters involved. Moreover, the extension of the model to propagating spin waves accounts for the measured frequency nonreciprocity, a quantity from which we extract a sixth magnetic parameter. The value of the latter is eventually refined by confronting frequency nonreciprocity data to full micromagnetic calculations.

The above ferromagnetic resonance study suggests that the entire thickness series can be described quite accurately with a thickness independent set of magnetic parameters. The exchange stiffness constant we determined lies within the range of values reported in literature for Fe at room temperature $A = 19$–23 pJ/m [39–41] and agrees particularly well with the recent determinations by Niitsu [40] and Kuz'min *et al.* [41]. The measured cubic anisotropy constant, on the other hand, is slightly larger than the values measured on bulk iron and thin iron films ($K_1 = 44$–$49\,\mathrm{kJ/m^3}$) [42–45], but it agrees well with results from first principles calculations ($K_1 = 52\,\mathrm{kJ/m^3}$) [45].

The third volume parameter, namely the uniaxial anisotropy K_U, accounts for the difference between the saturation magnetization M_s determined from SQUID magnetometry and the so-called effective magnetization $M_{\mathrm{eff}} = (M_s - H_U)$ measured from FMR. Now, we argue that this anisotropy originates from a distortion of the iron lattice. Indeed, the –4% mismatch between Fe and the MgO substrate is known to relax only partly through a dense array of dislocations formed in the first Fe atomic layers, thus leaving a small residual strain in nanometer thick films [46]. Accordingly, a tetragonal distortion is measured in the samples under study consisting of a 0.7% mean in-plane expansion and a 0.5% out-of-plane compression [22]. Such vertical lattice compression is expected to enhance the spin-orbit mediated interactions between electronic states, which favor an in-plane orientation of the magnetization [47]. To relate phenomenologically this extra magnetic anisotropy to the measured lattice distortion one may use the magnetoelastic coupling constants of bulk iron [48]. The obtained uniaxial anisotropy constant $K_U = -41\,\mathrm{kJ/m^3}$ (see Sander [49] for calculation details) is in very good agreement with our experimental observations regarding both its sign and its magnitude.

In terms of total perpendicular surface anisotropy, our results (see Table II) agree well with what is expected for an Fe ultrathin film sandwiched between two MgO layers [13–17]. From the joint results of broadband FMR and spin wave propagation, we can extract the values for the two individual PSA constants: $K_S^{\mathrm{bot}} = (K_S + \Delta K_S)/2 = 1.55\ \mathrm{mJ/m^2}$ for the bottom interface (MgO buffer/Fe) and $K_S^{\mathrm{top}} = (K_S - \Delta K_S)/2 = 0.75\ \mathrm{mJ/m^2}$ for the top one (Fe/MgO capping). These two values are within the range for the PSA obtained by ab-initio calculations [13–17] and measurements on ultrathin films with a single MgO/Fe interface [10–12,50,51]. However, in these previous experimental papers, the extracted values always included the contributions from two interfaces, and some hypothesis based on reference interfaces (e.g., V/Fe) needed to be included to extract individual values. In the present study we provide individual K_S values for both interfaces, which allows us to compare them directly with results from *ab initio* simulations and evidence that the ultrathin interface physics can be extrapolated to thicker films [10–17,50,51].

It has been shown theoretically that over/under oxidation at the Fe/MgO interface reduce drastically its surface anisotropy [15,16]. Moreover, using Mossbaüer spectroscopy, it has been shown that the Fe/MgO and MgO/Fe interfaces of a film can exhibit different amount of interfacial Fe oxidation [52]. Therefore, we attribute the difference in PSA at the two interfaces to a difference in their oxidation states. We assume that the distinct temperature treatments to which the bottom and top interfaces are subjected during growth is the reason for that: the 480 °C annealing, performed just after iron deposition, promotes a better epitaxy and higher value of surface anisotropy for the bottom MgO/Fe interface [12]. On the other hand, the top interface is not annealed, which likely leads to an over oxidation of the interfacial Fe atoms and a lower value of the PSA [15,16]. This behavior is corroborated by the larger value of ΔK_S observed in the 20 nm* sample without Ti protection (see blue dots in Fig. 6). For this sample, indeed, we argue that a further oxidation of the top interface may take place after the unprotected 8-nm thick MgO capping layer is exposed to water [53,54] both during the fabrication of this specific device and later under ambient conditions.

V. CONCLUSIONS

The magnetization dynamics of a thickness series of MgO/Fe(t)/MgO epitaxial films ($t = 10 - 30$ nm) was characterized using a combination of ferromagnetic resonance and nonreciprocal spin wave propagation measurements. Our rather versatile Kittel model accounts consistently for the frequencies of the uniform mode of magnetization precession and also for the inhomogeneous first standing spin wave mode. Noticeably, the ability to probe both of these modes over a wide range of film thicknesses allowed us to determine the exchange stiffness constant and the perpendicular surface anisotropy, two quantities, which are inaccessible through the sole study of homogeneous dynamics.

With our detailed ferromagnetic resonance characterization, we evidenced that the entire thickness series can be described with a single set of magnetic parameters. The magnetic volume parameters, cubic anisotropy and exchange stiffness, agree very well with what is expected for bulk iron. Also, an additional uniaxial perpendicular anisotropy was identified and attributed to a slight tetragonal distortion of the Fe lattice. Finally, it was possible to separate contributions of individual film interfaces to the perpendicular surface anisotropy with the help of complementary propagating spin wave spectroscopy measurements. The sizable asymmetry between the top and bottom interfaces was attributed to the different oxidation states of each interface. Our characterization suggest that 10–30 nm thick single crystalline Fe films have a well defined quasi-bulk magnetic interior, while the interfaces with MgO retain the large perpendicular surface anisotropy found in ultrathin film.

Our paper provides new light into the technologically-relevant ferromagnet/MgO interfaces and their effect on spin waves, while it also validates a new method for characterizing magnetic interfaces. Note that our methodology could be extended to alloys or multilayer systems, for which it could provide key information about possible inhomogeneities/asymmetries of the magnetic properties across the film thickness.

ACKNOWLEDGMENTS

We thank Arnaud Boulard, Benoît Leconte, Daniel Spor, Jérémy Thoraval, and Fares Abiza for assembling and testing the broadband FMR setup; Jérôme Robert for SQUID magnetometry measurements; Romain Bernard, Sabine Siegwald, and Hicham Majjad for technical support during nanofabrication work in the STnano platform; and Matías Grassi for useful discussion. We acknowledge financial support by the Interdisciplinary Thematic Institute QMat, as part of the ITI 2021-2028 Program of the University of Strasbourg, CNRS and Inserm, IdEx Unistra (ANR 10 IDEX 0002), SFRI STRAT'US Project (ANR 20 SFRI 0012) and ANR-17-EURE-0024 under the framework of the French Investments for the Future Program. We also acknowledge financial support from Region Grand Est through its FRCR call (NanoTeraHertz and RaNGE projects) and from Agence Nationale de la Recherche (France) under Contract No. ANR-20-CE24-0012 (MARIN).

APPENDIX A: DYNAMIC MATRICES

To find the resonance frequencies of the magnetization modes one has to solve the Landau-Lifshitz (LL) equation. For this, we substitute Eq. (2) for the static field, Eq. (7) for the dynamic field, and Eq. (4) for the dynamic magnetization into the linearized LL Eq. (1) and project the latter onto the space of cosine thickness modes, as explained in Sec. II [31]. To be able to derive useful analytical solutions, it is convenient to restrict this projection to the first two modes, yielding a total of four basis vectors $[\Phi_0\hat{\mathbf{x}},\ \Phi_1(\xi)\hat{\mathbf{x}},\ \Phi_0\hat{\mathbf{y}},\ \Phi_1(\xi)\hat{\mathbf{x}}]$ (two modes per spacial coordinate of the dynamic magnetization). After projection, the linearized LL equation [Eq. (1)] takes the form of an eigenvalue equation: $i\omega\bar{\mathbf{m}}^* = C\bar{\mathbf{m}}^*$, where C is the so called dynamic matrix, which in the present case, is 4×4 [29]. The eigenvalues of this matrix are the resonance frequencies and the eigenvectors describe the corresponding dynamic magnetization mode amplitudes. In Eq. (A1), we provide expressions for the dynamic matrices in cases where the external magnetic field is applied in-plane ($C_\parallel$) and out-of-plane ($C_\perp$).

$$C_\parallel = \gamma\mu_\mathrm{o}\begin{pmatrix} 0 & H_\parallel(k)+M_\mathrm{s}P_{00}(k) & -iM_\mathrm{s}Q(k) & 0 \\ -[H_\parallel(k)-H_\mathrm{U}-H_\mathrm{S}+M_\mathrm{s}[1-P_{00}(k)]] & 0 & -\frac{2\sqrt{2}\Delta K_\mathrm{S}}{\mu_\mathrm{o}tM_\mathrm{s}} & iM_\mathbf{s}Q(k) \\ iM_\mathrm{s}Q(k) & 0 & 0 & H_\parallel(k)+H_\mathrm{E}+M_\mathbf{s}P_{11}(k) \\ -\frac{2\sqrt{2}\Delta K_\mathrm{S}}{\mu_\mathrm{o}tM_\mathbf{s}} & -iM_\mathbf{s}Q(k) & -[H_\parallel(k)+H_\mathrm{E}-H_\mathrm{U}-2H_\mathrm{S}+M_\mathbf{s}[1-P_{11}(k)] & 0 \end{pmatrix} \tag{A1a}$$

$$C_\perp = \gamma\mu_\mathrm{o}\begin{pmatrix} 0 & H_\perp(k)+M_\mathbf{s}P_{00}(k) & 0 & -\frac{2\sqrt{2}\Delta K_\mathrm{S}}{\mu_\mathrm{o}tM_\mathrm{s}} \\ -H_\perp(k) & 0 & \frac{2\sqrt{2}\Delta K_\mathrm{S}}{\mu_\mathrm{o}tM_\mathrm{s}} & 0 \\ 0 & -\frac{2\sqrt{2}\Delta K_\mathrm{S}}{\mu_\mathrm{o}tM_\mathrm{s}} & 0 & H_\perp(k)+H_\mathrm{E}+H_\mathrm{S}+M_\mathbf{s}P_{11}(k) \\ \frac{2\sqrt{2}\Delta K_\mathrm{S}}{\mu_\mathrm{o}tM_\mathrm{s}} & 0 & -[H_\perp(k)+H_\mathrm{E}+H_\mathrm{S}] & 0 \end{pmatrix} \tag{A1b}$$

The fields $H_\parallel(k) = H + H_\mathrm{K} + M_\mathrm{s}\Lambda^2k^2$ and $H_\perp(k) = H + H_\mathrm{K} + H_\mathrm{U} + H_\mathrm{S} + M_\mathrm{s}(\Lambda^2k^2\text{-}1)$ are intermediate parameters introduced to simplify those expressions. $P_{00}(k) = 1 - \frac{1-e^{-|k|t}}{|k|t}$ and $P_{11}(k) = \frac{(kt)^2}{\pi^2+(kt)^2}(1 - \frac{2(kt)^2}{\pi^2+(kt)^2}\frac{1+e^{-|k|t}}{|k|t})$ are self demagnetizing factors for the cosine thickness modes $n = 0$ and $n = 1$, and $Q = \frac{\sqrt{2}kt}{\pi^2+(kt)^2}(1 + e^{-|k|t})$ is a mutual demagnetizing factor responsible for hybridization between those modes; all three factors being part of the magnetostatic Green's function that describes the dipolar interaction [37].

APPENDIX B: EFFECT OF A NONZERO ΔK_S ON THE STIFFNESS FIELDS IN THE CASE OF FERROMAGNETIC RESONANCE

In Sec. II we have derived Eq. (5) for the resonance frequencies of the modes $n = 0, 1$ by considering the effect of ΔK_S only up to first order. In the infinite wavelength limit ($k = 0$), those frequencies become fully independent of ΔK_S. Now, we proceed to consider the approximation up to second order in this parameter and study its effect on Eq. (5).

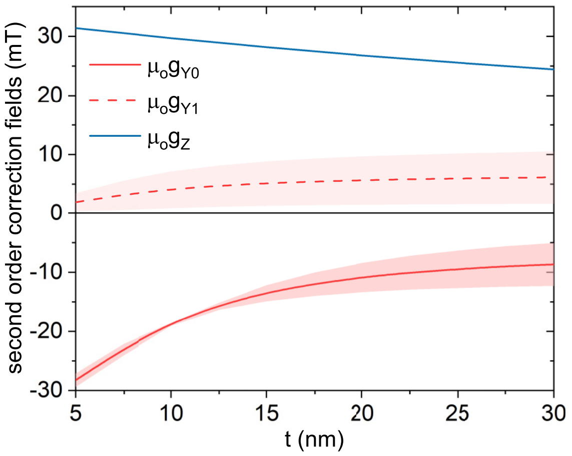

FIG. 7. Second-order correction functions for the stiffness fields [Eq. (B1)] as calculated with $\Delta K_S = 1.65$ mJ/m^2 to obtain a sizable effect. Functions g_{Yn} and g_Z are the stiffness field corrections for in-plane applied field, while g_Z applies to the out-of-plane case. The shaded zones around the lines account for the variations of $g_{\alpha n}$ with applied magnetic field in the range 0–1.3 T.

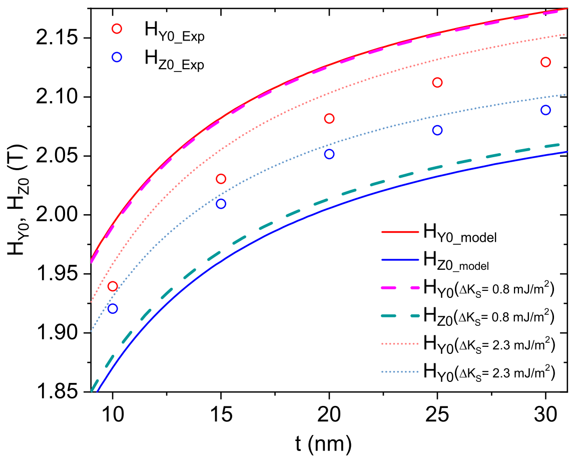

FIG. 8. Stiffness fields H_{Y0} (red) and H_{Z0} (blue) as functions of the Fe film thickness t. The open circles are the experimentally determined values and the lines are predictions of our analytical approach. Continuous, dashed, and dotted lines correspond, respectively, to first-order approximation, second-order approximation with $\Delta K_S = 0.8$ mJ/m^2, and second-order approximation with $\Delta K_S = 2.3$ mJ/m^2.

When keeping terms proportional to ΔK_S^2 in the model, the stiffness fields need to be modified as follows: $H_{Xn} \to H_{Xn}$, $H_{Yn} \to H_{Yn} + g_{Yn}$, $H_{Z0} \to H_{Z0} + g_Z$, and $H_{Z1} \to H_{Z1} - g_Z$, where the field corrections g_{Yn} ($n = 0$, 1) and g_Z are given by

$$g_{Y0}(H,t) = \frac{-8\frac{H_E+H_K+H}{(\mu_0 M_s t)^2}\Delta K_S^2}{H_S(H_K+H)+H_E[H_U-M_s-H_E+2(H_S-H_K-H)]}, \tag{B1a}$$

$$g_{Y1}(H,t) = \frac{8\frac{H_K+H}{(\mu_0 M_s t)^2}\Delta K_S^2}{H_S(H_K+H)+H_E[H_U-M_s-H_E+2(H_S-H_K-H)]}, \tag{B1b}$$

$$g_Z(t) = \frac{8\Delta K_S^2}{(\mu_0 M_s t)^2(H_E+H_S)}. \tag{B1c}$$

g_Z is completely independent of the external field H and g_{Yn} depends only very weakly on it in the range of interest (Fig. 7) so that it can also be considered as constant. Therefore, under this second-order approximation, the resonance frequencies $f_{\parallel n}$ and $f_{\perp n}$ retain approximately the Kittel-like form of Eq. (5), with the external field dependence contained entirely in the explicit H term. This justifies our fitting of the ferromagnetic resonance frequencies in Fig. 2 to Eq. (5) even in the presence of a sizable ΔK_S. We note in passing that, given their smallness (Fig. 7), the correction fields will have a negligible effect on the determination of the main parameters K_S and K_U.

As mentioned in the main text (Sec. II D), moving to second-order approximation allows one to improve qualitatively the agreement between theoretical and experimental values of the stiffness fields (Fig. 8). However, when assuming the value $\Delta K_S = 0.8$ mJ/m^2 determined from spin wave spectroscopy (Sec. III) the improvement remains marginal, especially regarding H_{Y0}, and only a much bigger value of ΔK_S allows one reaching a reasonably good matching (note the different vertical scales in Figs. 3 and 8). Here again, we evidence the tendency of our analytical approach to underestimate the effect of a difference in surface anisotropies. We attribute this quantitative discrepancy partially to the hypothesis made in writing Eq. (4), which is to neglect higher order terms in the Fourier series. We overcome this limitation with our numerical analysis (SWIMM code), which allows us to obtain a better overall agreement with broadband FMR and PSWS (see dotted and dashed lines in Figs. 3 and 8).

---

[1] H. Meng and J.-P. Wang, Spin transfer in nanomagnetic devices with perpendicular anisotropy, Appl. Phys. Lett. **88**, 172506 (2006).

[2] T. Kishi, H. Yoda, T. Kai, T. Nagase, E. Kitagawa, M. Yoshikawa, K. Nishiyama, T. Daibou, M. Nagamine, M. Amano *et al.*, Lower-current and fast switching of a perpendicular tmr for high speed and high density spin-transfer-torque MRAM, in *IEEE International Electron Devices Meeting, 2008* (IEEE, Piscataway, NJ, 2008) pp. 1–4.

[3] S. Ikeda, K. Miura, H. Yamamoto, K. Mizunuma, H. D. Gan, M. Endo, S. Kanai, J. Hayakawa, F. Matsukura, and H. Ohno, A perpendicular-anisotropy CoFeB-MgO magnetic tunnel junction, Nat. Mater. **9**, 721 (2010).

[4] W. Kim, J. H. Jeong, Y. Kim, W. C. Lim, J. H. Kim, J. H. Park, H. J. Shin, Y. S. Park, K. S. Kim, S. H. Park *et al.*, Extended scalability of perpendicular stt-mram towards sub-20nm MTJ node, in *IEEE International Electron Devices Meeting (IEDM), 2011* (IEEE, Piscataway, NJ, 2011) pp. 24.1.1–24.1.4.

[5] M. G. Moinuddin, A. H. Lone, S. Shringi, S. Srinivasan, and S. K. Sharma, Low-current-density magnetic tunnel junctions for STT-RAM application using Mgo$_x$ N$_{1-x}$ ($x = 0.57$) tunnel barrier, IEEE Trans. Electron Devices **67**, 125 (2020).

[6] M. T. Johnson, R. Jungblut, P. J. Kelly, and F. den Broeder, Perpendicular magnetic anisotropy of multilayers: Recent insights, J. Magn. Magn. Mater. **148**, 118 (1995).

[7] M. T. Johnson, P. J. H. Bloemen, F. J. A. d. Broeder, and J. J. d. Vries, Magnetic anisotropy in metallic multilayers, J. Phys. Soc. Jpn. **59**, 1409 (1996).

[8] T. Maruyama, Y. Shiota, T. Nozaki, K. Ohta, N. Toda, M. Mizuguchi, A. A. Tulapurkar, T. Shinjo, M. Shiraishi, S. Mizukami *et al.*, Large voltage-induced magnetic anisotropy change in a few atomic layers of iron, Nat. Nanotechnol. **4**, 158 (2009).

[9] Y. Shiota, T. Maruyama, T. Nozaki, T. Shinjo, M. Shiraishi, and Y. Suzuki, Voltage-assisted magnetization switching in ultrathin Fe 80 Co 20 alloy layers, Appl. Phys. Express **2**, 063001 (2009).

[10] C.-H. Lambert, A. Rajanikanth, T. Hauet, S. Mangin, E. E. Fullerton, and S. Andrieu, Quantifying perpendicular magnetic anisotropy at the Fe-MgO(001) interface, Appl. Phys. Lett. **102**, 122410 (2013).

[11] J. W. Koo, S. Mitani, T. T. Sasaki, H. Sukegawa, Z. C. Wen, T. Ohkubo, T. Niizeki, K. Inomata, and K. Hono, Large perpendicular magnetic anisotropy at Fe/MgO interface, Appl. Phys. Lett. **103**, 192401 (2013).

[12] J. Okabayashi, J. W. Koo, H. Sukegawa, S. Mitani, Y. Takagi, and T. Yokoyama, Perpendicular magnetic anisotropy at the interface between ultrathin Fe film and MgO studied by angular-dependent x-ray magnetic circular dichroism, Appl. Phys. Lett. **105**, 122408 (2014).

[13] R. Shimabukuro, K. Nakamura, T. Akiyama, and T. Ito, Electric field effects on magnetocrystalline anisotropy in ferromagnetic Fe monolayers, Phys. E **42**, 1014 (2010).

[14] K. Nakamura, T. Akiyama, T. Ito, M. Weinert, and A. J. Freeman, Role of an interfacial FeO layer in the electric-field-driven switching of magnetocrystalline anisotropy at the Fe/Mgo interface, Phys. Rev. B **81**, 220409(R) (2010).

[15] H. X. Yang, M. Chshiev, B. Dieny, J. H. Lee, A. Manchon, and K. H. Shin, First-principles investigation of the very large perpendicular magnetic anisotropy at Fe | MgO and Co | MgO interfaces, Phys. Rev. B **84**, 054401 (2011).

[16] A. Hallal, H. X. Yang, B. Dieny, and M. Chshiev, Anatomy of perpendicular magnetic anisotropy in Fe/MgO magnetic tunnel junctions: First-principles insight, Phys. Rev. B **88**, 184423 (2013).

[17] D. Odkhuu, W. S. Yun, S. H. Rhim, and S. C. Hong, Theory of perpendicular magnetocrystalline anisotropy in Fe/MgO (001), J. Magn. Magn. Mater. **414**, 126 (2016).

[18] V. W. Guo, B. Lu, X. Wu, G. Ju, B. Valcu, and D. Weller, A survey of anisotropy measurement techniques and study of thickness effect on interfacial and volume anisotropies in Co/Pt multilayer media, J. Appl. Phys. **99**, 08E918 (2006).

[19] S. Yakata, H. Kubota, Y. Suzuki, K. Yakushiji, A. Fukushima, S. Yuasa, and K. Ando, Influence of perpendicular magnetic anisotropy on spin-transfer switching current in CoFeB/MgO/CoFeB magnetic tunnel junctions, J. Appl. Phys. **105**, 07D131 (2009).

[20] L. E. Nistor, B. Rodmacq, C. Ducruet, C. Portemont, I. L. Prejbeanu, and B. Dieny, Correlation between perpendicular anisotropy and magnetoresistance in magnetic tunnel junctions, IEEE Trans. Magn. **46**, 1412 (2010).

[21] M. Yamanouchi, R. Koizumi, S. Ikeda, H. Sato, K. Mizunuma, K. Miura, H. D. Gan, F. Matsukura, and H. Ohno, Dependence of magnetic anisotropy on MgO thickness and buffer layer in Co_{20} Fe_{60} B_{20} -MgO structure, J. Appl. Phys. **109**, 07C712 (2011).

[22] G. C. Magnifouet Tchinda, Study of epitaxial Fe/Cr multilayers: Structural and magnetic properties, interdiffusion mechanisms, Ph.D. thesis, University of Strasbourg, 2020.

[23] R. N. Simons, G. E. Ponchak, K. S. Martzaklis, and R. R. Romanofsky, Channelized coplanar waveguide: Discontinuities, junctions, and propagation characteristics, in *IEEE MTT-S International Microwave Symposium Digest* (IEEE, Long Beach, CA, USA, 1989), Vol. 3, pp. 915–918.

[24] M. Bailleul, Shielding of the electromagnetic field of a coplanar waveguide by a metal film: Implications for broadband ferromagnetic resonance measurements, Appl. Phys. Lett. **103**, 192405 (2013).

[25] C. Bilzer, Microwave susceptibility of thin ferromagnetic films: Metrology and insight into magnetization dynamics, Ph.D. thesis, Université Paris Sud - Paris XI, 2007.

[26] K. J. Kennewell, M. Kostylev, N. Ross, R. Magaraggia, R. L. Stamps, M. Ali, A. A. Stashkevich, D. Greig, and B. J. Hickey, Magnetization pinning at a Py/Co interface measured using broadband inductive magnetometry, J. Appl. Phys. **108**, 073917 (2010).

[27] C. Kittel, On the theory of ferromagnetic resonance absorption, Phys. Rev. **73**, 155 (1948).

[28] A. Hubert and R. Schäfer, *Magnetic domains: The analysis of magnetic microstructures* (Springer, Berlin, 2014).

[29] O. Gladii, M. Haidar, Y. Henry, M. Kostylev, and M. Bailleul, Frequency nonreciprocity of surface spin wave in permalloy thin films, Phys. Rev. B **93**, 054430 (2016).

[30] A. Gurevich and G. Melkov, *Magnetization Oscillations and Waves* (CRC Press, Boca Raton, FL, 1996).

[31] B. A. Kalinikos and A. N. Slavin, Theory of dipole-exchange spin wave spectrum for ferromagnetic films with mixed exchange boundary conditions, J. Phys. C **19**, 7013 (1986).

[32] B. A. Kalinikos, M. P. Kostylev, N. V. Kozhus, and A. N. Slavin, The dipole-exchange spin wave spectrum for anisotropic ferromagnetic films with mixed exchange boundary conditions, J. Phys.: Condens. Matter **2**, 9861 (1990).

[33] J. N. Solano Córdova, Broadband ferromagnetic resonance characterization for CoFeB, Py, YIG thin films and Py/YIG bilayer system, B.S. thesis, Universidad San Francisco de Quito, 2017.

[34] M. Kostylev, Non-reciprocity of dipole-exchange spin waves in thin ferromagnetic films, J. Appl. Phys. **113**, 053907 (2013).

[35] V. Vlaminck and M. Bailleul, Spin-wave transduction at the submicrometer scale: Experiment and modeling, Phys. Rev. B **81**, 014425 (2010).

[36] O. Gladii, D. Halley, Y. Henry, and M. Bailleul, Spin-wave propagation and spin-polarized electron transport in single-crystal iron films, Phys. Rev. B **96**, 174420 (2017).

[37] K. Y. Guslienko and A. N. Slavin, Magnetostatic Green's functions for the description of spin waves in finite rectangular magnetic dots and stripes, J. Magn. Magn. Mater. **323**, 2418 (2011).

[38] Y. Henry, O. Gladii, and M. Bailleul, Propagating spin-wave normal modes: A dynamic matrix approach using plane-wave demagnetizating tensors, arXiv:1611.06153.

[39] T. Devolder, T. Tahmasebi, S. Eimer, T. Hauet, and S. Andrieu, Compositional dependence of the magnetic properties of

epitaxial FeV/MgO thin films, Appl. Phys. Lett. **103**, 242410 (2013).

[40] K. Niitsu, Temperature dependence of magnetic exchange stiffness in iron and nickel, J. Phys. D **53**, 39LT01 (2020).

[41] M. D. Kuz'min, K. P. Skokov, L. V. B. Diop, I. A. Radulov, and O. Gutfleisch, Exchange stiffness of ferromagnets, Euro. Physical J. Plus **135**, 1 (2020).

[42] K. H. J. Buschow, *Encyclopedia of Materials: Science and Technology* (Elsevier, Amsterdam, 2001).

[43] C. D. Graham, Magnetocrystalline anisotropy constants of iron at room temperature and below, Phys. Rev. **112**, 1117 (1958).

[44] B. Westerstrand, P. Nordblad, and L. Nordborg, The magnetocrystalline anisotropy constants of iron and iron-silicon alloys, Phys. Scr. **11**, 383 (1975).

[45] I. Barsukov, S. Mankovsky, A. Rubacheva, R. Meckenstock, D. Spoddig, J. Lindner, N. Melnichak, B. Krumme, S. I. Makarov, H. Wende, H. Ebert, and M. Farle, Magnetocrystalline anisotropy and Gilbert damping in iron-rich $Fe_{1-x}Si_x$ thin films, Phys. Rev. B **84**, 180405(R) (2011).

[46] J. Du, H. Chen, C. Xu, Y. Fan, Y. Qiu, H. Wang, and E. Fu, Stress of misfit dislocation at Fe/MgO interface drives the annihilation of radiation induced defects, Acta Mater. **210**, 116798 (2021).

[47] R. Q. Wu, L. J. Chen, A. Shick, and A. J. Freeman, First-principles determinations of magneto-crystalline anisotropy and magnetostriction in bulk and thin-film transition metals, J. Magn. Magn. Mater. **177-181**, 1216 (1998).

[48] R. F. S. Hearmon, The elastic constants of anisotropic materials, Rev. Mod. Phys. **18**, 409 (1946).

[49] D. Sander, The magnetic anisotropy and spin reorientation of nanostructures and nanoscale films, J. Phys.: Condens. Matter **16**, R603 (2004).

[50] A. Kozioł-Rachwał, T. Giela, B. Matlak, K. Matlak, M. Ślęzak, T. Ślęzak, M. Zając, R. Rüffer, and J. Korecki, Magnetism of ultrathin fe films in MgO/Fe/MgO in epitaxial structures probed by nuclear resonant scattering of synchrotron radiation, J. Appl. Phys. **113**, 214309 (2013).

[51] A. Kozioł-Rachwał, W. Skowroński, T. Ślęzak, D. Wilgocka-Ślęzak, J. Przewoźnik, T. Stobiecki, Q. H. Qin, S. van Dijken, and J. Korecki, Room-temperature perpendicular magnetic anisotropy of MgO/Fe/MgO ultrathin films, J. Appl. Phys. **114**, 224307 (2013).

[52] E. Młyńczak, K. Freindl, N. Spiridis, and J. Korecki, Epitaxial Mgo/Fe(001) and Fe/Mgo(001): Structures of the interfaces, J. Appl. Phys. **113**, 024320 (2013).

[53] S. A. Holt, C. F. Jones, G. S. Watson, A. Crossley, C. Johnston, C. J. Sofield, and S. Myhra, Surface modification of mgo substrates from aqueous exposure: An atomic force microscopy study, Thin Solid Films **292**, 96 (1997).

[54] A. H. Youssef, G. Kolhatkar, A. Merlen, R. Thomas, and A. Ruediger, Surface preparation and the evolution of atomically flat step terrace morphology of MgO single crystals, AIP Adv. **8**, 095025 (2018).